



# Benchmarking the Degradation Behavior of Aluminum Foil Anodes for Lithium-Ion Batteries

Timothy Chen,<sup>[a]</sup> Akila C. Thenuwara,<sup>[a]</sup> Wendy Yao,<sup>[b]</sup> Stephanie Elizabeth Sandoval,<sup>[c]</sup> Congcheng Wang,<sup>[a]</sup> Dae Hoon Kang,<sup>[d]</sup> Diptarka Majumdar,<sup>[d]</sup> Rajesh Gopalaswamy,<sup>[d]</sup> and Matthew T. McDowell<sup>\*[a, c]</sup>

Aluminum is an attractive candidate for replacing graphite anodes in lithium-ion batteries because of its high specific capacity and the potential for direct use as foil. However, achieving reversible reaction of aluminum is challenging due to volume changes, SEI formation, and sluggish ion transport. Although prior work has investigated electrochemical transformation behavior of aluminum, the effects of key variables, including areal capacity per cycle and alloy composition, are not well understood. Here, we carry out comprehensive electrochemical testing to benchmark the performance of two different aluminum foils (99.999% Al and Al 8111). We find that for constant thickness, both foil compositions exhibit a power-law

dependence of cycle life on the lithiated areal capacity per cycle, revealing that degradation is significantly more rapid at higher areal capacities. This behavior is interpreted as an “electrochemical fatigue” mechanism, in analogy to mechanical fatigue. Additionally, the alloy composition was found to strongly affect the Coulombic efficiency (CE), with high-purity foils exhibiting higher initial CE but reduced long-term stability. Finally, *operando* optical microscopy revealed different spatio-temporal reaction mechanisms amongst the different materials. This improved understanding of aluminum foil anodes paves the way for efforts to engineer aluminum-based foils with enhanced stability.

## Introduction

Alloy anodes, such as silicon, tin, aluminum, and other materials, are promising candidates for replacing the graphite anode in lithium-ion batteries because of their high specific and volumetric  $\text{Li}^+$  storage capacity. These materials have been investigated and pursued for several decades.<sup>[1–4]</sup> Silicon-based alloy anodes have been extensively studied for the past 15 years, resulting in substantial scientific and technological progress.<sup>[5–7]</sup> However, this focus on silicon alloy anodes has somewhat overshadowed research interest on other alloy candidates, and one in particular – aluminum – has received comparatively minor research emphasis since initial explorations in the early 1970s.<sup>[8–10]</sup> Aluminum is an abundant material that alloys/de-alloys with lithium at low potentials ( $\sim 0.28 \text{ V}$  and  $\sim 0.45 \text{ V}$  vs.  $\text{Li}/\text{Li}^+$ , respectively) to form  $\text{LiAl}$ , and it features

almost three times the theoretical specific capacity of graphite<sup>[11]</sup> (990 vs. 372  $\text{mAh g}^{-1}$ ). This high specific capacity would enable the creation of battery cells with similar specific energy to that of silicon and other alloy materials (Figure 1). A key advantage of aluminum over other elements, including silicon, is that aluminum is already widely and cheaply manufactured as foils, and the possibility of directly incorporating foil-based anodes in Li-ion batteries could simplify manufacturing significantly compared to slurry processing.<sup>[12,13]</sup>

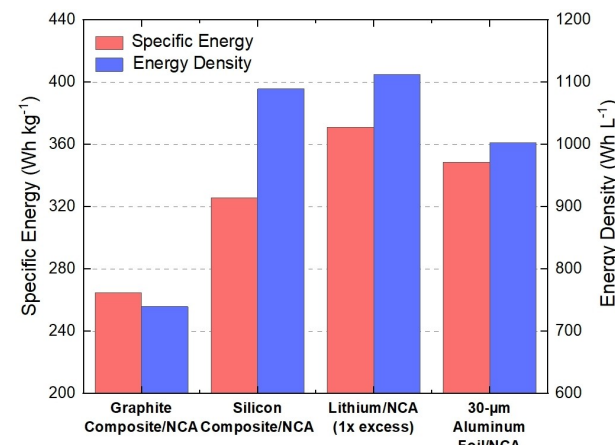


**Figure 1.** Stack-level energy density and specific energy comparison of Li-ion battery cells with different anode materials. The graphite, silicon, and lithium-based stacks include a copper anode current collector, while the aluminum-foil-based cell has excess foil at the anode and therefore has no anode current collector.  $\text{LiNi}_{0.8}\text{Co}_{0.15}\text{Al}_{0.05}\text{O}_2$  (NCA) composite cathodes with areal capacity of  $4.0 \text{ mAh cm}^{-2}$  are used for all cases. See Supporting Information for full calculation details.

[a] T. Chen, Dr. A. C. Thenuwara, Dr. C. Wang, Prof. Dr. M. T. McDowell  
George W. Woodruff School of Mechanical Engineering  
Georgia Institute of Technology  
Atlanta, GA, 30332 USA  
E-mail: mattmcowell@gatech.edu

[b] W. Yao  
School of Chemical and Biomolecular Engineering  
Georgia Institute of Technology  
Atlanta, GA, 30332 USA

[c] S. E. Sandoval, Prof. Dr. M. T. McDowell  
School of Materials Science and Engineering  
Georgia Institute of Technology  
Atlanta, GA, 30332 USA

[d] Dr. D. H. Kang, Dr. D. Majumdar, Dr. R. Gopalaswamy  
Novelis, Inc.  
Kennesaw, GA, 30144 USA

Supporting information for this article is available on the WWW under  
<https://doi.org/10.1002/batt.202200363>

Furthermore, a single foil could be used as both the active material and current collector. However, the lithiation and delithiation of aluminum induces volume changes of around 90%, which can cause mechanical degradation of foils and exacerbate solid-electrolyte interphase (SEI) growth.<sup>[11]</sup> The surface oxide layer can also inhibit lithium-ion transport, and poor initial Coulombic efficiency (CE) has often been observed.<sup>[11]</sup> These fundamental challenges ultimately led to graphite as the preferred anode in commercial lithium-ion batteries over aluminum in the early days of lithium-ion battery research.

Prior work on aluminum-based anodes has focused on modifying the composition to improve cyclability.<sup>[11]</sup> Combining aluminum with other elements that are inert or that actively alloy with lithium, such as zinc, tin, or silicon,<sup>[14]</sup> has been shown to be beneficial. These additions likely modify the volume change and structural degradation behavior of these alloy materials during lithiation/delithiation, thus improving chemo-mechanical stability. For instance, researchers have fabricated “interdigitated eutectic” foils via severe plastic deformation from cold rolling to create secondary phases.<sup>[13,15–18]</sup> These eutectic structures have shown extended cycling stability and relatively high capacity compared to pure aluminum. The key disadvantage is that introducing other elements may reduce the specific capacity compared to pure aluminum, and certain elemental additions in large quantities may increase cost.

Other studies have focused on modifying the surface of aluminum anodes. Coating the surface of aluminum with a protective layer, such as carbon black or graphene, has been shown to improve the growth of the SEI layer and to prevent pulverized aluminum from detaching from the anode.<sup>[11,19]</sup> In conjunction with this work, efforts to tailor liquid electrolytes have been shown to affect cycling behavior.<sup>[20]</sup> Bis(fluorosulfonyl)imide (FSI)-based salts within electrolytes have shown success in reducing overlithiation to prevent the formation of the  $\text{Li}_{1+x}\text{Al}$  phase, which is irreversible.<sup>[21,22]</sup> Electrolytes with a high salt concentration have also improved cycling stability and enabled higher discharge capacity.<sup>[23–25]</sup>

In addition to these engineering strategies, research has been dedicated to understanding the fundamental electrochemical reaction and material transformation behaviors of aluminum. Electrochemical lithiation at room temperature results in the formation of the  $\beta\text{-LiAl}$  phase as the maximally lithiated phase despite the phase diagram featuring phases with higher lithium content ( $\text{Li}_3\text{Al}_2$  and  $\text{Li}_9\text{Al}_4$ ).<sup>[11]</sup> Tahmasebi et al. showed that the lithiation of aluminum begins by nucleation of the  $\beta\text{-LiAl}$  phase on the surface, and these domains grow until they connect.<sup>[26]</sup> During delithiation, fracture of the  $\beta\text{-LiAl}$  phase can cause delamination from the pristine material, and dealloying induces pore formation in the delithiated material.<sup>[27,28]</sup> This delamination, as well as lithium trapping, have been proposed as possible mechanisms for capacity decay. Pre-lithiating the surface of aluminum may also help with alleviating stress concentrations during initial cycling.<sup>[29]</sup> The Vickers hardness of the aluminum has been reported to affect the uniformity of the lithiation reaction; if the

aluminum is too soft or too hard, then the lithiated aluminum has uneven nucleation across the surface.<sup>[30]</sup> Partial lithiation, instead of complete lithiation, has been shown to extend cycling stability of pure aluminum films because the brittle  $\beta\text{-LiAl}$  islands can expand into the softer, unreacted  $\alpha\text{-Al}$ .<sup>[18,26]</sup>

Despite recent converging interest and progress in aluminum anode research for Li-ion batteries, many fundamental questions remain unanswered. Although a variety of studies have sought to improve the performance of aluminum-based anodes and have compared aluminum-based eutectic alloys or composites to traditional graphite, the community has limited knowledge of the fundamental degradation behavior and reaction mechanisms of aluminum foils. There has not been systematic experimentation showing how the extent of reaction in each cycle of an aluminum foil affects electrochemical cyclability, or how the composition of the aluminum alloy that makes up the foil influences behavior. The extent of reaction (i.e., areal capacity or thickness of the lithiated region) per cycle, and its relationship to the overall foil thickness, is a critical value that will determine the energy density of battery cells. Most prior papers have cycled relatively low areal capacity per cycle (<1 mAh cm<sup>-2</sup>) while using very thick aluminum foils (>100  $\mu\text{m}$ );<sup>[14,26]</sup> neither are appropriate for commercial Li-ion batteries. Li-ion batteries require 2–4 mAh cm<sup>-2</sup> areal capacity, and aluminum anode thicknesses over ~50–60 microns would result in low energy density cells comparable to the use of conventional graphite. As such, there is little knowledge in the published literature regarding the behavior of aluminum under realistic cycling conditions. It is thus necessary to understand how cycling under a variety of realistic conditions affects degradation behavior to benchmark the performance of aluminum-foil-based anodes.

In this work, we seek to understand how the extent of reaction in each cycle influences the electro-chemo-mechanical degradation behavior of aluminum foils with different alloy compositions as anodes for Li-ion batteries. We present a comprehensive benchmarking dataset showing the electrochemical cycling stability of two different aluminum foils (high purity aluminum and aluminum alloy 8111). The data show that there is a strong dependence of CE on the initial composition of the aluminum alloy, with high-purity foils exhibiting much higher CE values in initial cycles. In addition, extensive testing of degradation behavior over a wide range of conditions reveals an approximate power-law dependence of cycle life on the extent of lithiation per cycle, which we propose can be interpreted as a universal “electrochemical fatigue” failure mechanism inspired by conventional mechanical fatigue failure processes. The degradation behavior occurs because additional aluminum is consumed via lithium reaction each cycle, which exposes increasing amounts of surface area to promote SEI formation, eventually leading to electrolyte exhaustion. We further characterize structural and morphological evolution of these various foils during cycling with *in situ* and *ex situ* techniques, showing that foil composition determines reaction uniformity. The new findings in this study regarding fundamental behavior of aluminum foil anodes provide an important foundation for further improvement of

aluminum foil active materials for next-generation Li-ion batteries.

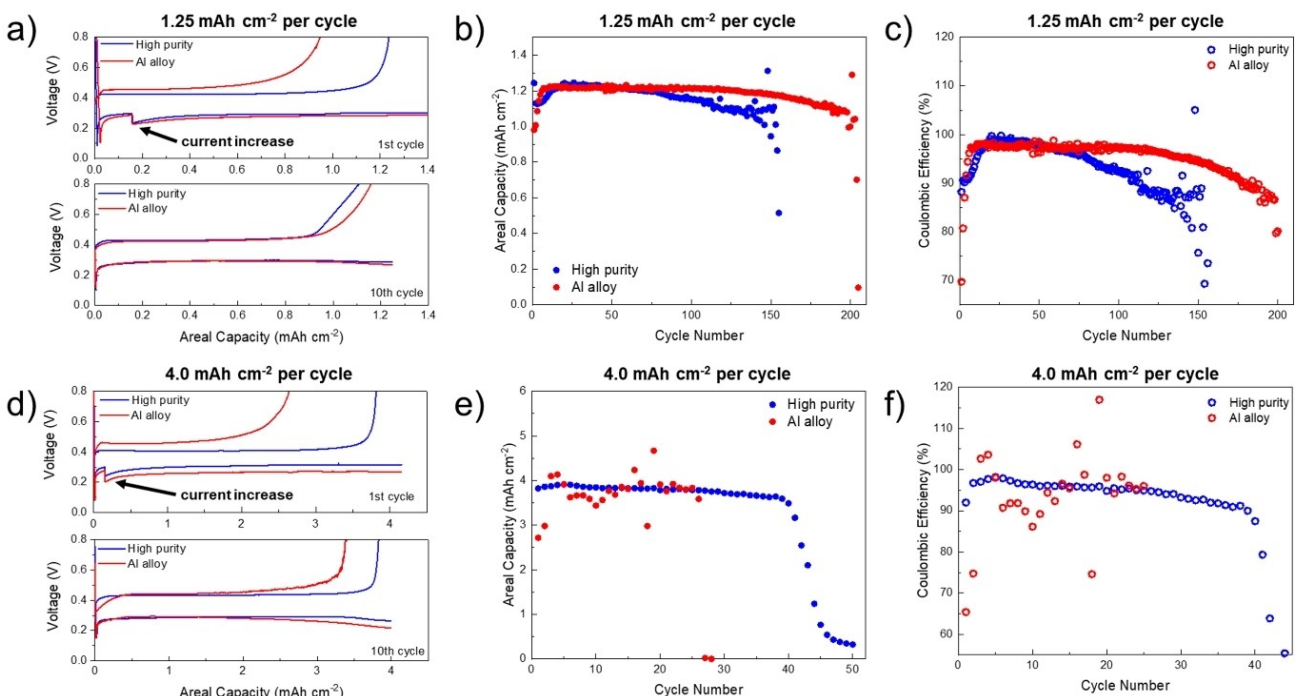
## Results and Discussion

High-purity aluminum and aluminum alloy foils were cycled in half-cells using various areal capacities per cycle. All the cells were initially lithiated using the relatively low current density of  $0.052 \text{ mA cm}^{-2}$  for 3 h. The current density was then increased to  $0.15 \text{ mA cm}^{-2}$  for the remaining duration of the first cycle before running all subsequent cycles at a current density of  $0.5 \text{ mA cm}^{-2}$ . Figure 2(a and d) shows typical voltage curves for cells that were cycled with areal capacities of  $1.25 \text{ mAh cm}^{-2}$  and  $4.0 \text{ mAh cm}^{-2}$  per cycle, respectively. Note that lithiating the full 30- $\mu\text{m}$  thickness of the foils would result in  $\sim 8 \text{ mAh cm}^{-2}$  areal capacity. For both areal capacities shown in Figure 2(a and d), the voltage curves for each foil composition are presented for the first (top panels) and tenth cycles (bottom panels). For the first cycle, the sharp drop in voltage signifies the overcoming of the nucleation overpotential, followed by plateau behavior around 0.25 V, which corresponds to the lithiation of aluminum to form  $\beta$ -LiAl. During charging, the voltage plateaus around 0.45 V during delithiation of the foils, and it then abruptly increases toward the end of delithiation. In the first cycle, the Coulombic efficiency (CE) varies strongly with the different types of foils ( $\sim 90\%$  for high-purity aluminum,  $\sim 65\%-70\%$  for aluminum alloy). These results are

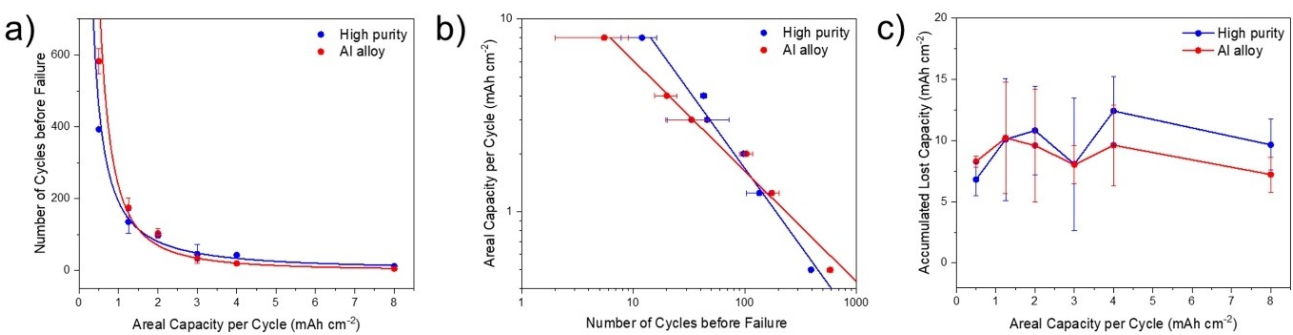
likely due to a greater extent of lithium trapping in the alloy foil compared to the high-purity foil.

Figure 2(b and e) shows the charge (delithiation) capacities with cycling when using controlled areal discharge capacities of  $1.25 \text{ mAh cm}^{-2}$  and  $4.0 \text{ mAh cm}^{-2}$ , respectively. Figure 2(c and f) shows the CEs for those same cells. For the cells cycled at  $1.25 \text{ mAh cm}^{-2}$  (Figure 2b), the delithiation capacities increase with cycling as the CE also increases. The capacity and CE values are then fairly stable for at least 100 cycles, followed by a rapid decrease of stored capacity over a few cycles, corresponding to cell failure. Similar behavior was observed for the cells cycled with areal capacity per cycle of  $4.0 \text{ mAh cm}^{-2}$ , but with more erratic capacity values and reduced cycles to failure. This rapid degradation behavior after fairly stable cycling was observed over many cells in our studies, and it contrasts with the steady degradation with cycling typically found in conventional electrodes for Li-ion batteries. The CE values when using the lower areal capacity of  $1.25 \text{ mAh cm}^{-2}$  (Figure 2c) are more stable than those at the higher areal capacity of  $4.0 \text{ mAh cm}^{-2}$  (Figure 2f). Figure S1 in the Supporting Information contains a similar dataset but for cycling with lower areal capacity ( $0.5 \text{ mAh cm}^{-2}$ ), where over 500 cycles were achieved for alloy foils.

Figure 3(a) shows a compilation of the electrochemical cycling stability behavior from an extensive collection of half cells under different cycling conditions. This plot shows the number of cycles before failure as a function of areal capacity per cycle. Each data point is the average value of multiple cells; a total of 60 cells were tested to failure for inclusion in this plot.



**Figure 2.** Typical electrochemical cycling behavior of two different aluminum foils: high-purity aluminum and 8111 aluminum alloy. a) First (top) and tenth (bottom) cycle voltage curves, b) areal capacity during delithiation, and c) Coulombic efficiencies using  $1.25 \text{ mAh cm}^{-2}$  per cycle. d) First (top) and tenth (bottom) cycle voltage curves, e) areal capacity during delithiation, and f) Coulombic efficiencies using  $4.0 \text{ mAh cm}^{-2}$  per cycle. Current densities were  $0.5 \text{ mA cm}^{-2}$  after an initial slower lithiation step.



**Figure 3.** Compiled electrochemical cycling behavior and electrochemical fatigue mechanism. a) Number of cycles before failure vs. the areal capacity per cycle for both types of foil; the number of cycles to failure exhibits a strong dependence on areal capacity. Each data point is the average of multiple cells run to failure, with the error bars showing standard deviation. b) Logarithmic plot of the data in (a) with the axes exchanged to show similarity to lifetime plots in mechanical fatigue analysis. Lines are linear fits. c) Accumulated lost capacity over the duration of cycling for each of the conditions in (a and b), in which the accumulated lost capacity is the sum of the Coulombic inefficiency over cycling.

The error bars represent the standard deviation of the number of cycles before failure. We defined failure based on the typical behavior as observed in Figure 2(b) to be when the attained delithiation capacity decreases permanently below 50% of the initial lithiation capacity. A few cells (especially those that underwent hundreds of cycles) exhibited significant excess delithiation capacities beyond the lithiation capacity likely due to short circuits; we excluded these cells from the analysis.

The compiled dataset in Figure 3(a) shows a distinctive trend in which the areal capacity per cycle strongly affects the number of cycles before failure. Both types of foil show approximately the same trend, with 400–600 cycles achieved when using  $0.5 \text{ mAh cm}^{-2}$ , which rapidly falls to  $\sim 100$  cycles before failure when using  $2.0 \text{ mAh cm}^{-2}$ . Notably, the alloy foil shows better cyclability compared to the high purity foil at low areal capacities ( $\sim 600$  cycles to failure vs  $\sim 400$  cycles to failure using  $0.5 \text{ mAh cm}^{-2}$ ). At even higher areal capacities ( $4.0$  and  $8.0 \text{ mAh cm}^{-2}$ ), the cells only cycled tens of times before failure. These compiled data represent an important result of our study, unequivocally demonstrating the significant impact of areal capacity on cycling stability for these aluminum foils. Indeed, many prior studies have used relatively low areal capacity values<sup>[21,25,31]</sup> which can enable extended cyclability, but such low values are insufficient for achieving the energy densities necessary for commercial cells.

Interestingly, the dataset in Figure 3(a) shows exponentially increasing cycle life as areal capacity is decreased. To demonstrate this, Figure 3(b) shows these same results on a plot with logarithmic axes, with the axes also exchanged. Each type of foil exhibits an approximately linear trend indicating a negative correlation between cycles before failure and the areal capacity per cycle. This can be fit with a power law relationship  $C = A(N)^b$ , where  $C$  is the areal capacity used per cycle,  $N$  is the number of cycles before failure,  $A$  is the prefactor, and  $b$  is the exponent. Fitting the curves from the two foil types in Figure 3(b) to a power law results in the extracted  $A$  and  $b$  values shown in Table 1. The high purity aluminum foil shows a more negative  $b$  exponent, which is caused by the lower cycling stability of high-purity aluminum at low areal capacities and slightly greater cycling stability at high areal capacities

**Table 1.** Fitted power law values from data in Figure 3(b).

Foil type	$A [\text{mAh cm}^{-2} \text{ cycle}^{-1}]$	$b$ [a.u.]
High Purity Al	67.83	-0.803
Al Alloy	22.79	-0.573

(Figure 3a and b). It is possible that this observation could be explained by differences in mechanical degradation between the foils during initial cycling (as discussed later), but this is not definitive.

The observation of the approximate power-law behavior in Figure 3(b), which corresponds to the strong influence of the extent of reaction per cycle on the number of cycles attained before failure, provides insight into the fundamental degradation mechanisms of aluminum-foil based materials. Specifically, we propose that these data can be interpreted as an “electrochemical fatigue” mechanism, as an analogue to conventional mechanical fatigue. Mechanical fatigue describes the accumulation of subtle mechanical damage (e.g., defect accumulation and plasticity) during cyclic stress application, which eventually results in dramatic mechanical failure, such as fracture. Mechanical fatigue with constant amplitude loading also obeys power-law behavior, such as the Coffin-Manson law,<sup>[32]</sup> which describes the relationship between the amplitude of inelastic strain per cycle on total stress cycles endured before failure:

$$\varepsilon = \varepsilon_f (2N_f)^c \quad (1)$$

Here,  $\varepsilon$  represents the amplitude of inelastic strain per cycle,  $2N_f$  represents the cycle life, and  $\varepsilon_f$  and  $c$  are constant values based on material properties. Logarithmic strain-life (S-N) plots show linear dependency and are used to predict the useful life of materials undergoing cyclic mechanical loading.

The similarity between the power law relationships in our electrochemical data and that of traditional mechanical fatigue merits a comparison between these cases. In the electrochemical testing of the foils, the extent of reaction per cycle (i.e., areal capacity per cycle) is similar to the cyclic stress amplitude in mechanical fatigue, but these processes cause different types of “damage” to accumulate. During each cycle

of lithium insertion and removal from the aluminum foil electrodes, a certain additional amount of the aluminum material is newly lithiated, since the Coulombic efficiency is not unity. The lithiation/delithiation of the foil causes new porosity to form, and as more of the foil becomes reacted each cycle, additional surface area is exposed to the electrolyte.<sup>[28]</sup> This process causes increasing amounts of SEI formation each cycle until eventually the electrolyte is entirely consumed, which corresponds to the rapid cell failure that is shown in Figure 2(b). Failure due to electrolyte consumption was confirmed by opening cells after failure and adding new electrolyte, which allowed cycling to resume with high capacity (Supporting Information Figure S2). The measured CE values, such as in Figure 2(c), support this mechanism, as the CE initially increases to be close to 100% over tens of cycles, but then steadily decreases toward the end of life, corresponding to incrementally increasing SEI formation throughout the porous foil.

Analysis of the accumulated amount of "lost capacity" in Figure 3(c) further supports these conclusions. The plot in Figure 3(c) was constructed by summarizing the Coulombic inefficiency (1-CE) from each cycle over the duration of cycling for each cell. Figure 3(c) shows that the average values over many cells are approximately constant with some scatter. This finding suggests that regardless of areal capacity per cycle, when a certain amount of electrolyte is consumed, the cells fail. In this electrochemical analogue to mechanical fatigue, then, it is the accumulation of electrochemical damage in the form of incrementally increasing surface area every cycle that drives steadily increasing SEI growth, eventually leading to catastrophic failure via electrolyte exhaustion. We note that the increasing surface area and thus SEI growth every cycle is distinct from conventional particulate electrodes in which the surface area is approximately constant throughout cycling. This behavior is unique to foils that have fresh unreacted material beneath a reacted region, where the unreacted material can be incrementally consumed each cycle to generate new porosity that is exposed to the electrolyte."

Figure 4 shows further analysis of the electrochemical cycling data. Figure 4(a) shows the average cumulative lithiation capacities of the foils across all cycles from the dataset in Figure 3(a). From this plot, larger cumulative capacities are achieved for both foil types when smaller areal capacities are

used per cycle; this trend is especially pronounced for the alloy foil. This finding is counter to the alternative scenario in which the cumulative capacity would be the same regardless of areal capacity used, which would be expected if incremental damage per cycle (i.e., internal surface exposure and SEI growth) was linearly dependent on the amount of charge passed. Instead, it is clear that larger areal capacities cause more extensive damage to accumulate each cycle, leading to the exponentially reduced cycle life shown in Figure 3(a and b). This behavior supports the comparison to mechanical fatigue, where larger mechanical stress amplitudes (the analogy to areal capacity) cause significantly more damage to accumulate each cycle.

Figure 4(b) shows the average first-cycle CE values for the two types of foils as a function of areal capacity with cycling (Figure S3 shows similar data for cycling at lower current densities, with similar results). The high purity foil exhibits much higher initial CE (85%–90%, vs. 55%–80% for the alloy). We speculate that the lower initial CEs of the alloy foil may arise from Li trapping at inclusions and secondary phases. Figure 4(c) shows the average CE over the first 10 cycles for all cells that lasted longer than ten cycles. High-purity aluminum still shows higher average CE compared to the aluminum alloy. Although high-purity aluminum shows superior CE in initial cycles, this does not necessarily extend to longer cycling in half cells, as the CE decreases for high-purity aluminum in later cycles.

To explore the physical mechanisms behind the electrochemical performance of these aluminum foil anodes, we performed SEM characterization of the foils cycled at 2.0 mAh cm<sup>-2</sup> after cycling, as shown in Figure 5. Each subfigure of Figure 5 shows an optical photograph, a cross-sectional SEM image, and a top-down SEM image of foils after one cycle (Figure 5a, c) or 10 cycles (Figure 5b, d). After one cycle, the photographs show that the foil electrodes are still intact, while the SEM cross sections show that unreacted aluminum is present beneath a reacted layer. The top-down SEM images show that holes are present in the reacted layer of the high-purity aluminum (Figure 5a). This is different than the aluminum alloy, which exhibits crack patterns in the reacted layer at the surface (Figure 5c). This mechanical damage occurs because of the stress evolution during volume changes due to lithiation/delithiation. The holes in the high purity aluminum

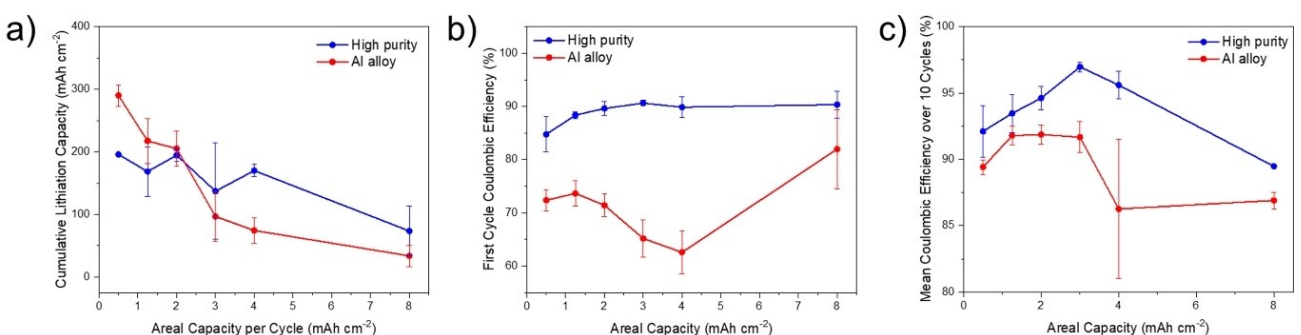
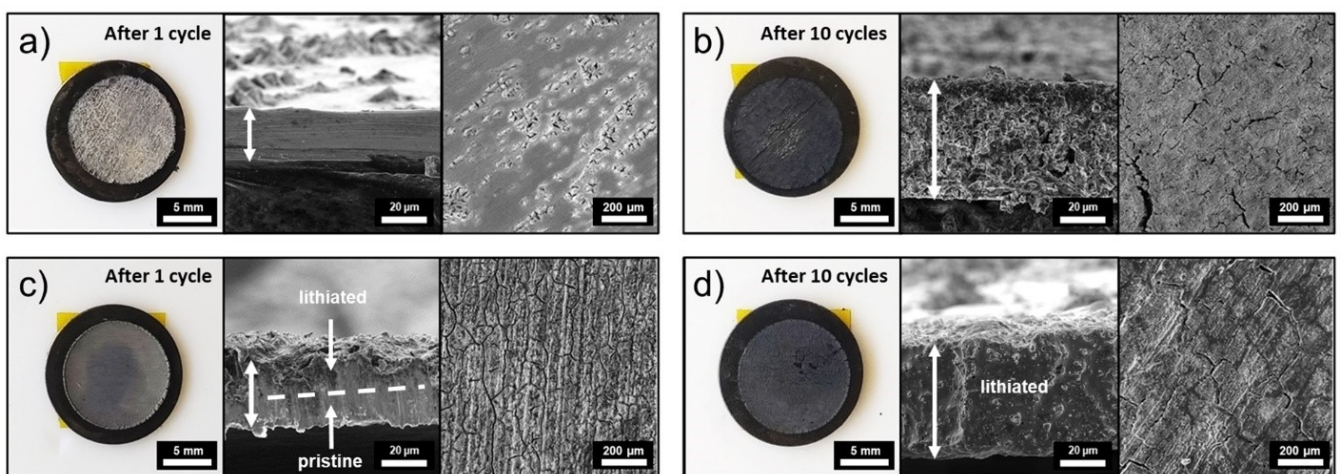


Figure 4. Further analysis of electrochemical cycling of aluminum foils. (a) Cumulative lithiation capacity vs. areal capacity per cycle. (b) Average first-cycle CE vs. areal capacity per cycle. (c) Average CE over first 10 cycles vs. areal capacity per cycle.



**Figure 5.** Morphology evolution of Al foils after cycling. Each subfigure includes an optical photograph, a cross-section SEM image, and a top-down SEM image. a, b) High-purity Al after a) 1 cycle and b) 10 cycles. c, d) Al alloy after c) 1 cycle and d) 10 cycles. Each cycle used  $2.0 \text{ mAh cm}^{-2}$  areal capacity.

likely arise from localized stress concentrations due to non-uniform reaction behavior. The more uniform fracture of the alloy foil suggests that lithiation/delithiation is more uniform across the surface, resulting in uniformly distributed fracture. After 10 cycles (Figure 5b, d) the photographs of the electrodes show macroscale cracks and significant damage. The SEM cross sections show that the foils are highly reacted, and the high-purity foil (Figure 5b) shows significant porosity. The top-down SEM images also show more substantial fracture. We note that this observed mechanical damage should not be interpreted as directly causing the “electrochemical fatigue” mechanism discussed previously, despite the analogy to mechanical fatigue. Instead, we have concluded that it is the formation of internal porosity during cycling (such as that in Figure 5b) that leads to increased surface area and accelerated SEI formation.

To understand the uniformity of the reaction processes in the different foils, we carried out *in situ* optical microscopy experiments (see Methods for details). Figure 6 shows the optical cell imaging for high-purity (Figure 6a) and alloy (Figure 6b) foils. For each sample in Figure 6, an image is shown in the pristine state (left), after lithiation with  $1.0 \text{ mAh cm}^{-2}$  inserted, and after delithiation. SEM images of the same samples after delithiation are included as well to show higher-magnification views of the surface. The most notable finding from these experiments is that the high-purity aluminum foil undergoes nonuniform lithiation and delithiation, with greater extent of reaction in some regions that causes a hole to form after delithiation (Figure 6a, right side). The surface of the aluminum alloy reacts much more uniformly, forming distributed cracks after delithiation rather than holes (Figure 6b). This

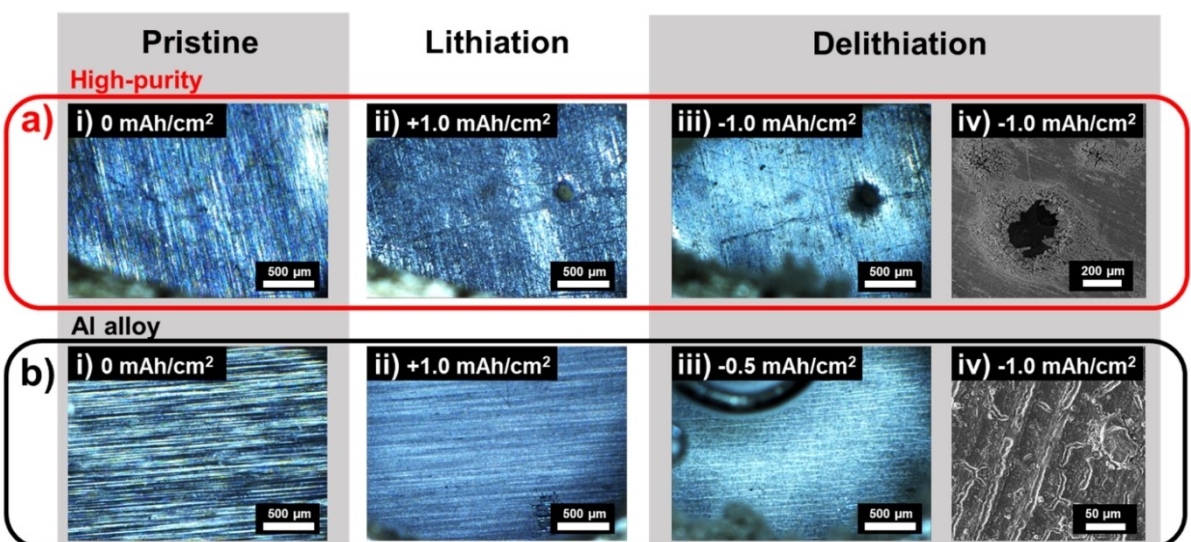


**Figure 6.** *In situ* optical microscopy experiments of the lithiation/delithiation of Al foils. a) high-purity Al and b) Al alloy foil under optical cell testing. i) pristine; ii) lithiated; iii) delithiated. iv) shows SEM images of the foils after delithiation.

is consistent with the *ex situ* imaging in Figure 5. The cracks that form in the aluminum alloy resemble “mud cracking” due to tensile stress generation during delithiation, which has previously been reported in battery materials experiencing large strains.<sup>[18,33]</sup> We note that the *in situ* microscopy involves reaction of foils without applied stack pressure, which is different than the coin cell results displayed previously. Regardless, the finding of nonuniform reaction in high purity foils here is consistent with their behavior in coin cells (Figure 5). The differences between the high purity and alloy foils likely occur due to different nucleation behavior of the  $\beta$ -LiAl. The addition of alloying elements thus appears to enable a more uniform distribution of  $\beta$ -LiAl to form, which is likely beneficial for managing chemo-mechanical evolution during cycling.

We also carried out X-ray diffraction (XRD) to understand the phase evolution in the different aluminum foils. Previous studies have shown that the  $\beta$ -LiAl phase is the terminally lithiated phase although  $\text{Li}_3\text{Al}_2$  and  $\text{Li}_9\text{Al}_4$  are found on the phase diagram, but these phases are not generally observed upon lithiation room temperature.<sup>[11]</sup> Figure 7 shows XRD results of high-purity and aluminum alloy foils after lithiation with an areal capacity of  $2.0 \text{ mAh cm}^{-2}$ . The peaks in the pristine sample data (aluminum alloy) correspond to the face-

centered cubic (fcc) aluminum diffraction pattern. Peaks from fcc-Al and  $\beta$ -LiAl are present in the spectra of the lithiated foils. The high-purity foil shows particularly high peak intensities for the aluminum peaks with respect to  $\beta$ -LiAl, likely because of nonuniform spatial lithiation as seen in Figures 5 and 6. Overall, these results confirm that both aluminum foils are indeed undergoing lithiation to form  $\beta$ -LiAl, although they do not preclude the presence of amorphous lithiated phases.

As a final component of this work, we fabricated relatively large ( $\sim 25 \text{ cm}^2$  electrode area) single-layer pouch cells for demonstration of aluminum anode cycling behavior in full cells. Figure 8 shows the electrochemical performance of an aluminum alloy paired with an LFP cathode with  $1.25 \text{ mAh cm}^{-2}$  areal capacity in such a pouch cell. Figure 8(a) shows the voltage curves for the 1<sup>st</sup>, 2<sup>nd</sup>, and 10<sup>th</sup> cycles, Figure 8(b) shows its cycling stability, and Figure 8(c) shows the CE with cycling. There is a significant drop in cell capacity over the first few cycles due to the relatively low CE of the aluminum anode in these cycles, but the CE rapidly increases to  $>97\%$ . The cell then shows relatively stable cycling but with low areal capacity ( $\sim 0.3 \text{ mAh cm}^{-2}$ ). This is consistent with our findings from half cells that the aluminum foils are much more stable when using lower areal capacities per cycle. These data show that full cells can be cycled with good stability when using low areal capacities in comparison to the overall theoretical capacity of the foil, which has often been seen in the literature.<sup>[21,25,31]</sup> The key challenge for aluminum-based anodes is to achieve commercially-relevant areal capacities ( $2\text{--}4 \text{ mAh cm}^{-2}$ ) in foils that are as thin as possible (30 microns or less) to enable high energy density.

## Conclusion

This investigation has revealed the nature of electrochemical cycling when using different aluminum alloy foils under varying extents of reaction during cycling. Aluminum foil anodes for Li-ion batteries offer the possibility of achieving high energy density and specific energy, but only if high areal capacities (approaching  $4 \text{ mAh cm}^{-2}$ ) and thin foils are used. We have demonstrated that the areal capacity per cycle plays a key role in determining cycle life of aluminum foil anodes, with lower

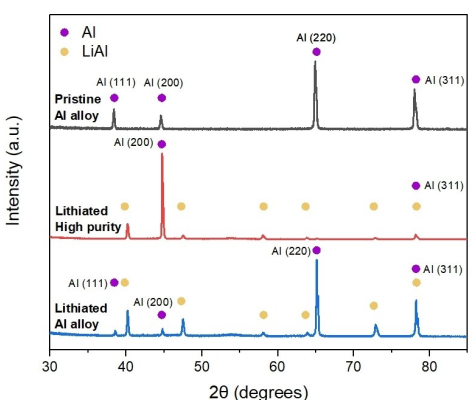


**Figure 7.** *Ex-situ* XRD of aluminum foils after lithiation with  $2.0 \text{ mAh cm}^{-2}$  areal capacity. The pristine foil in black is aluminum alloy foil that has not been lithiated. JCPDS cards 04–0787 (Al) and 03–1215 (AlLi) were used to analyze the peaks.

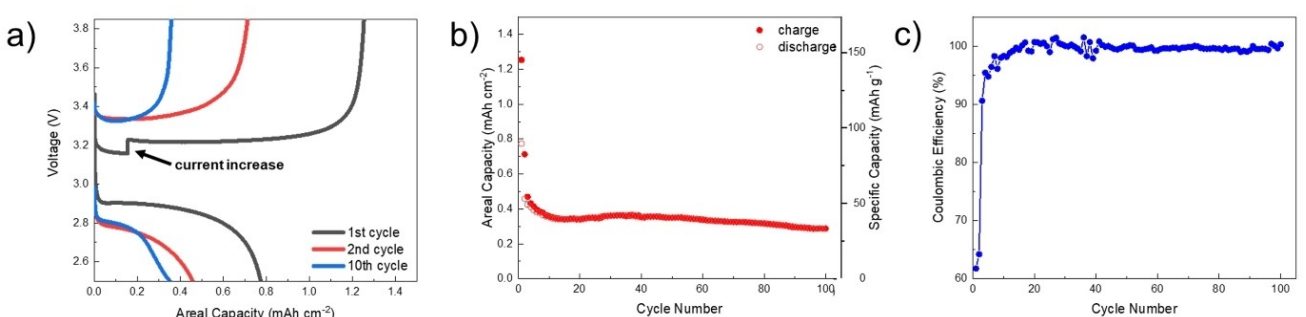


**Figure 8.** Electrochemical cycling of single-layer LFP/Al alloy pouch cell with  $25 \text{ cm}^2$  electrode area. a) Voltage curves, b) areal capacity with cycling, and c) CE with cycling.

areal capacities exponentially extending cycle life. Based on extensive testing of half cells, we propose an “electrochemical fatigue” mechanism that governs aluminum foil degradation behavior, which is manifest by an approximate power-law relationship between the cycle life and the extent of reaction per cycle (i.e., the areal capacity). This degradation mechanism is an electrochemical analogue to conventional mechanical fatigue, which exhibits similar power law relationships between the number of stress cycles and the stress amplitude. Both mechanisms involve the subtle accumulation of “damage” every cycle, be it plasticity and defect accumulation in mechanical fatigue or incrementally increasing SEI growth due to greater exposed surface area every cycle in electrochemical fatigue. We note that such a mechanism could also be found in conventional particulate electrodes, but it is particularly evident in these foil experiments because of the ease of utilizing different areal capacities per cycle, and the additional material that is reacted every cycle that promotes excessive SEI formation. In addition to this identified mechanism, we show that the different foil compositions exhibit different early-stage average CE values, with high-purity foil showing much higher CE than the aluminum alloy foil over the first few cycles. Furthermore, the different foils show different spatial uniformity of lithiation/delithiation reaction processes, resulting in different mechanical degradation characteristics.

Overall, our results show that the key challenge in developing aluminum foil anodes for Li-ion batteries is to achieve high areal capacity per cycle while undergoing stable long-term cycling. To achieve this, the performance of foils would have to break free of the power law stability-area capacity curve shown in Figure 3b. Such performance can potentially be achieved by altering the foil microstructure or composition to minimize excess surface area generated during cycling, which promotes SEI growth. Furthermore, optimization of the electrolyte could also be beneficial. Future efforts can use the results and conclusions of this study to benchmark the behavior and performance of engineered aluminum-based anodes on the way to improved performance.

## Materials and Methods

**Aluminum materials:** 30-μm thick foils of high-purity aluminum (99.999% Al, Laurand Associates) and an aluminum alloy (~98.5% Al, 0.61–0.64% Si, 0.47–0.72% Fe, 0.002% Cr, 0.002–0.01% Cu, 0.007% Ga, 0.02% Mg, 0.003–0.007% Mn, 0.005% Ni, 0.03% Ti, 0.01% V, 0.002–0.006% Zn, <0.001% Zr; produced by Hindalco Industry Ltd. and donated by Novelis, Inc.) were used in this study. This aluminum alloy composition corresponds to AA8111. Two different 8111 foils were used with different Fe content; one contained 0.47% Fe and the other contained 0.72% Fe. There was no observable difference in electrochemical behavior, reaction processes, or cycle life between these two AA 8111 foils, and thus data from both are grouped herein as “aluminum alloy.”

**Coin cell assembly:** 9.5-mm or 12-mm diameter foils were assembled into half-cells with Celgard separators inside a Vigor glove box with  $O_2$  and  $H_2O < 1$  ppm. The electrolyte used in this study was 1.0 M lithium difluoro(oxalate)borate (LiDFOB, Sigma Aldrich) and 1.0 M lithium bis(fluorosulfonyl)imide (LiFSI, Fischer

Scientific) in 3:7 fluoroethylene carbonate:diethyl carbonate (FEC: DEC) by volume (Sigma Aldrich). This electrolyte was developed through a systematic procedure to optimize cycling duration of aluminum anodes and showed improved cycling performance over conventional electrolytes such as LiPF<sub>6</sub> salts in carbonates. In each coin cell, two separators were soaked in electrolyte and an additional 50 μL of electrolyte was added.

**Pouch cell assembly:** Single-layer pouch cells were assembled inside an MBraun glove box with  $O_2$  and  $H_2O < 1$  ppm. Aluminum alloy foils (26.10 cm<sup>2</sup> area) were paired with LiFePO<sub>4</sub> (LFP, 24.08 cm<sup>2</sup> area, NEI Corp.) then assembled in single-layer pouch cells. The LFP cathodes had an areal capacity of 1.25 mAh cm<sup>-2</sup>. 2 mL of the same electrolyte used for the coin cells were used (1.0 M LiDFOB, 1.0 M LiFSI in 3:7 FEC:DEC by volume). A stack pressure of 0.5 MPa was applied to the pouch cells during galvanostatic testing.

**Electrochemical testing:** Electrochemical testing was performed using Arbin and Landt battery testers. For the coin-type half cells, a 3-h initial lithiation step with a low current density of 0.052 mA cm<sup>-2</sup> was applied before galvanostatic cycling. The first galvanostatic cycle was then performed with a current density of 0.15 mA cm<sup>-2</sup>, and then all subsequent cycles used a current density of 0.5 mA cm<sup>-2</sup>. Galvanostatic cycling was performed on half cells with voltage limits of 0.01 V and 1.0 V, and during lithiation (discharge), a time limit was applied to determine the extent of partial lithiation per cycle. Half-cells were tested with areal capacities per cycle of 1.25 mAh cm<sup>-2</sup>, 2.0 mAh cm<sup>-2</sup>, 3.0 mAh cm<sup>-2</sup>, 4.0 mAh cm<sup>-2</sup>, and 8.0 mAh cm<sup>-2</sup>. For reference, the 30-μm thick foils tested herein have a maximum areal capacity of 8.04 mAh cm<sup>-2</sup>. Full-cell testing was performed between 2.5 V and 3.85 V. The first activation cycle was run at C/20, and then all subsequent cycles were run at C/10 fully with no partial lithiation.

**Scanning electron microscopy:** Scanning electron microscopy (SEM) was performed with a Tescan Mira3 XM FEG-SEM instrument. Images of the foils were collected top-down and in cross-section after one cycle of lithiation/delithiation and after ten cycles of lithiation/delithiation with areal capacity per cycle of 2.0 mAh cm<sup>-2</sup>.

**X-ray diffraction:** X-ray diffraction (XRD) data were collected on a Panalytical Empyrean instrument using a copper X-ray source ( $K\alpha$  of 1.54184 Å). Patterns were collected with a  $2\theta$  range of 20° to 80°. Samples were mounted on a reflection-transmission spinner stage. Lithiated samples used a glass slide as a substrate and were encased in mylar. XRD was performed for both pristine aluminum foil and foils lithiated to an areal capacity of 2.0 mAh cm<sup>-2</sup>.

**In-situ optical microscopy:** Custom optical microscopy cells were assembled inside a Vigor glovebox.<sup>[34]</sup> A ring of lithium metal with 0.16 cm<sup>2</sup> area and aluminum foil with 0.32 cm<sup>2</sup> area were each mounted to separate glass slides. A 1.6-mm thick O-ring was placed between the two glass slides and the assembly was compressed tightly together with a clamp. 0.2 mL of electrolyte (1.0 M LiDFOB, 1.0 M LiFSI with 3:7 FEC:DEC by volume) was injected into the system through the O-ring with a syringe.

The optical microscopy cells were then removed from the glove box and cycled while viewing with an optical microscope using a Bio-Logic VMP3 potentiostat. Pre-lithiation at a current density of 0.052 mA cm<sup>-2</sup> was carried out for 10 min, then lithiation and delithiation steps were performed each to 1.0 mAh cm<sup>-2</sup> at a current density of 0.5 mA cm<sup>-2</sup> for a single cycle. Video microscopy of the experiments was recorded using a custom-built microscope (Edmund Optics) at 2× magnification using a Mitutoyo infinity-corrected lens with a working distance of 34 mm.

**Foil chemical analysis:** Chemical analysis was performed with inductively coupled plasma testing, with a confidence level of +/−0.02 w/w%.

## Acknowledgements

Support is acknowledged from Novelis, Inc. S.E.S. acknowledges support from an NSF Graduate Research Fellowship under Grant No. DGE-1650044 and a Sloan Foundation MPH Program Scholarship. This work was performed in part at the Georgia Tech Institute for Electronics and Nanotechnology, a member of the National Nanotechnology Coordinated Infrastructure (NNCI), which is supported by the National Science Foundation (ECCS-2025462). The authors thank Hindalco Industries Ltd for supplying the alloy foils.

## Conflict of Interest

Some of the authors are inventors on a provisional patent application related to aluminum materials for Li-ion batteries.

## Data Availability Statement

Supporting Information includes details regarding calculations for Figure 1, as well as supplementary figures. Data from the paper are available from the corresponding author upon reasonable request.

**Keywords:** alloy anodes • aluminum • batteries • electrochemistry • energy storage

- [1] W. J. Zhang, *J. Power Sources* **2011**, *196*, 13.
- [2] W. J. Zhang, *J. Power Sources* **2011**, *196*, 877.
- [3] M. T. McDowell, F. J. Quintero Cortes, A. C. Thenuwara, J. A. Lewis, *Chem. Mater.* **2020**, *32*, 8755.
- [4] B. T. Heligman, A. Manthiram, *ACS Energy Lett.* **2021**, *6*, 2666.
- [5] M. T. McDowell, S. W. Lee, W. D. Nix, Y. Cui, *Adv. Mater.* **2013**, *25*, 4966.
- [6] A. Franco Gonzalez, N. H. Yang, R. S. Liu, *J. Phys. Chem. C* **2017**, *121*, 27775.
- [7] L. Sun, Y. Liu, R. Shao, J. Wu, R. Jiang, Z. Jin, *Energy Storage Mater.* **2022**, *46*, 482.
- [8] A. N. Dey, *J. Electrochem. Soc.* **1971**, *118*, 1547.

- [9] M. R. Kelegman, *Voltaic cells with lithium-aluminum alloy anode and nonaqueous solvent electrolyte system*, US Patent US3639174 A, **1970**.
- [10] J. O. Besenhard, G. Eichinger, *J. Electroanal. Chem. Interfacial Electrochem.* **1976**, *68*, 1.
- [11] H. Wang, H. Tan, X. Luo, H. Wang, T. Ma, M. Lv, X. Song, S. Jin, X. Chang, X. Li, *J. Mater. Chem. A* **2020**, *8*, 25649.
- [12] S. T. Boles, M. H. Tahmasebi, *Joule* **2020**, *4*, 1342.
- [13] K. J. Kreder, B. T. Heligman, A. Manthiram, *ACS Energy Lett.* **2017**, *2*, 2422.
- [14] M. H. Tahmasebi, D. Kramer, H. Geßwein, T. Zheng, K. C. Leung, B. T. W. Lo, R. Möning, S. T. Boles, *J. Mater. Chem. A* **2020**, *8*, 4877.
- [15] A. Manthiram, K. J. Kreder III, B. T. Heligman, *Multiphase Metal Foils as Integrated Metal Anodes for Non-Aqueous Batteries*, US Patent no. US11380886B2, **2018**.
- [16] B. T. Heligman, K. J. Kreder, A. Manthiram, *Joule* **2019**, *3*, 1051.
- [17] K. Srikantha Prabanna Balan, K. Shah, J. Yu, B. T. Heligman, A. Manthiram, V. R. Subramanian, G. S. Hwang, K. Muthuraman, *ECS Meeting Abstracts 2021, MA2021-01*, 384.
- [18] S. S. Sharma, P. J. Crowley, A. Manthiram, *ACS Sustainable Chem. Eng.* **2021**, *9*, 14515.
- [19] M. Jiang, Y. Yu, H. Fan, H. Xu, Y. Zheng, Y. Huang, S. Li, J. Li, *ACS Appl. Mater. Interfaces* **2019**, *11*, 15656.
- [20] S. P. Kuksenko, *Russ. J. Electrochem.* **2013**, *49*, 67.
- [21] B. Qin, S. Jeong, H. Zhang, U. Ulissi, D. Carvalho, A. Varzi, S. Passerini, *ChemSusChem* **2019**, *12*, 208.
- [22] B. Qin, T. Diemant, H. Zhang, A. Oefling, R. J. Behm, J. Tübke, A. Varzi, S. Passerini, *ChemSusChem* **2019**, *12*, 2609.
- [23] Z.-H. Chang, J.-T. Wang, Z.-H. Wu, M. Gao, S.-J. Wu, S.-G. Lu, *ChemSusChem* **2018**, *11*, 1787.
- [24] Y. Yamada, A. Yamada, *J. Electrochem. Soc.* **2015**, *162*, A2406.
- [25] A. K. Chan, R. Tatarra, S. Feng, P. Karayaylali, J. Lopez, I. E. L. Stephens, Y. Shao-Horn, *J. Electrochem. Soc.* **2019**, *166*, A1867.
- [26] M. H. Tahmasebi, D. Kramer, R. Möning, S. T. Boles, *J. Electrochem. Soc.* **2019**, *166*, A5001.
- [27] T. Zheng, D. Kramer, M. H. Tahmasebi, R. Möning, S. T. Boles, *ChemSusChem* **2020**, *13*, 974.
- [28] T. Zheng, D. Kramer, M. H. Tahmasebi, R. Möning, S. T. Boles, *ChemSusChem* **2020**, *13*, 5910.
- [29] D. Li, F. Chu, Z. He, Y. Cheng, F. Wu, *Mater. Today* **2022**, *58*, 80–90.
- [30] H. Li, T. Yamaguchi, S. Matsumoto, H. Hoshikawa, T. Kumagai, N. L. Okamoto, T. Ichitsubo, *Nat. Commun.* **2020**, *11*, 1584.
- [31] T. Zheng, D. Kramer, R. Möning, S. T. Boles, *ACS Sustainable Chem. Eng.* **2022**, *10*, 3203.
- [32] J. Bannantine, J. Comer, J. Handrock, *Fundamentals of Metal Fatigue Analysis*, Prentice Hall, Englewood Cliffs, N. J., **1990**.
- [33] L. Y. Beaulieu, K. W. Eberman, R. L. Turner, L. J. Krause, J. R. Dahn, *Electrochem. Solid-State Lett.* **2001**, *4*, A137.
- [34] S. E. Sandoval, F. J. Q. Cortes, E. J. Klein, J. A. Lewis, P. P. Shetty, D. Yeh, M. T. McDowell, *J. Electrochem. Soc.* **2021**, *168*, 100517.

Manuscript received: August 16, 2022

Revised manuscript received: September 29, 2022

Accepted manuscript online: September 30, 2022

Version of record online: November 3, 2022